Appl. Phys. B 70, 287–294 (2000) / Digital Object Identifier (DOI) 10.1007/s003409900116

Applied Physics B
Lasers
and Optics

Characterisation of a spark ignition system by planar laser-induced fluorescence of OH at high repetition rates and comparison with chemical kinetic calculations

A. Dreizler[1], S. Lindenmaier[1], U. Maas[1], J. Hult[2], M. Aldén[2], C.F. Kaminski[2]

[1] Institut für Technische Verbrennung, Universität Stuttgart, Pfaffenwaldring 12, 70569 Stuttgart, Germany
(Fax: +49-711/685-5653, E-mail: dreizler@itv.uni-stuttgart.de)
[2] Lund Institute of Technology, Department of Physics, Division of Combustion Physics, P.O. Box 118, 22100 Lund, Sweden
(Fax: +46-46/2224542, E-mail: clemens.kaminski@forbrf.lth.se)

Received: 6 April 1999/Published online: 27 October 1999

Abstract. This study reports the application of a novel, high speed laser-detector system for the time-resolved study of flame propagation in a well-controlled spark ignition system. The ignition system allowed full and reproducible control over the energy deposited during breakdown and the ensuing arc discharge of the spark plasma. Ignition was performed in a closed vessel which was filled with stoichiometric mixtures of methane and air. Four sequential snapshots of two-dimensional OH distributions were recorded during single ignition events by the use of planar laser-induced fluorescence (PLIF). From these OH distributions flame front velocities have been extracted with an accuracy of better than 2%. One-dimensional numerical simulations of the ignition event including detailed chemistry and transport processes have been performed. Experimental results and results from the simulations have been compared to each other with respect to flame front velocities as well as spatial concentration profiles of OH radicals. In general a good agreement was obtained. In this way the ignition system was carefully characterised.

PACS: 07.50.-e; 07.60.-j; 47.11.+j

In many technical applications an electrical spark initiates a combustion process. A detailed knowledge of the chemistry and physics of the ignition and the subsequent flame propagation in its different modes is necessary to optimise, for example, the design of igniters used in lean-operation I.C. engines [1–3]. On the other hand, this knowledge is for example of great importance concerning the prevention of accidental ignitions in the chemical industry [4] or in atomic power plants [5].

The present study reports on a detailed investigation and characterisation of spark-ignited combustion events. The flame propagation in premixed methane–air mixtures under precisely defined conditions was studied by means of planar laser-induced fluorescence (PLIF) of the OH radical. Furthermore, the system was investigated by numerical simulations and detailed comparisons with the experimental results were carried out. The conditions under which the present investigations were performed are sufficiently general to aid an improvement in the understanding of a wide variety of problems of technical and academic interest.

A typical electrical spark of commercial ignition systems can be divided into three phases [6]. First, a short breakdown phase is initiated which creates a conducting plasma channel between two electrodes. Temperatures in this phase have been reported to reach up to 60 000 K [6]. Owing to the high pressure increase inside the plasma channel a shock wave is generated which leaves the activated volume within approximately 1 μs. This shock wave heats the surrounding gas it passes through [7–9]. After the formation of the plasma channel, the charge stored in the electrodes (which act like a capacitor) is discharged very rapidly (in the order of ns) [10]. The high conductivity of the plasma channel causes a drop in electrical resistance and the arc phase is initiated. This second phase is characterised by a much lower potential drop and temperature (up to 6000 K [6]). When the cathode fall is building up, the glow phase begins. Typically temperatures decrease to approximately 3000 K in this third phase of the spark ignition process. The conversion efficiency from electrical to thermal energy of the gas phase decreases from the breakdown to the glow phase [11] because of heat loss to the electrodes.

At the surface of the plasma channel a layer of highly reactive radicals and atoms is formed at high temperatures giving rise to a growing flame kernel. A few hundred μs after the breakdown the surface temperature is lower than 3000 K [6]. For this range the "high-temperature chemistry" of hydrocarbon combustion applies for the description of the ensuing ignition process [12]. The further development of this initial flame kernel is of course influenced by a variety of parameters. Depending on stoichiometry, heat losses to the electrodes, and the turbulence intensity of the load the flame kernel may extinguish, a self-sustaining flame propagation (deflagration) may ensue, or a detonation may develop.

Spark ignition has been investigated by a number of researchers in closed vessels [6, 7, 13–15] and in flow reactors [16, 17]. An excellent survey of early investigations is given in [18]. In more recent work [6] the initiation and subsequent flame propagation by breakdown, arc, and glow phase were investigated for a variety of different CH_4–air mixtures

using time-resolved interferometry. A review of spark ignition concepts which enable an efficient transfer of electrical into thermal energy of the gas phase has been given in [2] with an emphasis on lean-burn operation of stratified Otto engines.

The overall aim of this research is to provide a database for a sufficiently large number of single ignition events which is necessary for detailed comparisons with mathematical models simulating the process. The purpose of the present study is to characterise an electric ignition system specifically designed to deliver highly reproducible spark ignition. The reproducibility of the system was verified by state-of-the-art, time-resolved PLIF imaging of OH radicals during early stages of the flame development. Simultaneously, the deposition of electrical energy into the system was measured in real time by suitable current and voltage probes. The experimental results concerning the size of the flame kernel as well as speeds of flame propagation were modelled mathematically. The importance of chemical reactions and molecular transport on the ignition process has been highlighted in detail in [14]. The model employed here takes, within a one-dimensional approximation, full chemistry and detailed transport phenomena into account. The experimental approach used here allowed us, for the first time, to deduce flame speeds from OH concentration fields as they develop in real time. Possible perturbations of the flame development could thus be studied directly in a time-resolved way. This was crucially important for subsequent work by the present group where experiments were performed to study the interaction of chemistry and turbulence under well-defined conditions, using the same ignition system as characterised here [19].

The paper begins with a short review of the strategy employed to describe the ignition and fate of the flame kernel mathematically. Then the design of the ignition system and combustion vessel as well as the set-up of the PLIF spectrometer are presented. Results from experiments as well as numerical calculations are shown and compared to each other. Finally, conclusions are drawn from these findings and an outlook to forthcoming activities is given.

1 Simulation of ignition and flame propagation

A one-dimensional representation of the spark ignition and flame propagation process was employed in the present study. For this approach, a cylindrical geometry of the spark channel was assumed which is in close agreement to the shape of the spark actually observed by imaging the luminous emission from the plasma. The spark was assumed to be an infinite cylinder with radius r_s. Influences of the electrodes (i.e. heat conduction) were not accounted for. Calculations were performed in a radial direction outwards from the axis of the spark channel. Although PLIF data is two-dimensional in nature, only data along this axis were compared with the simulations. The formation of a shock wave by the short breakdown was neglected, the justification for this simplification is given in the following section.

The ignition process as well as subsequent flame propagation were simulated mathematically by solving the conservation equations for total mass, species masses, momentum, and energy, as detailed in [20]. The conservation equations are closed by using the ideal gas law and a detailed multispecies transport model based on the Curtiss–Hirschfelder approximation [21]. The system of ordinary differential, as well as algebraic, equations resulting after spatial discretization was solved using the program package LIMEX [22]. Computations were performed on a workstation (Silicon Graphics) with a R4000 processor.

The spark was modelled by an energy source term given by

$$q = \frac{D_s}{\tau_s} \exp\left\{-\left(\frac{r}{r_s}\right)^8\right\} \quad \text{for} \quad 0 \le t \le \tau_s \tag{1}$$

and

$$q = 0 \quad \text{for} \quad t > \tau_s\,. \tag{2}$$

Here D_s denotes the energy density, τ_s represents the duration, and r_s the radius of the spark. This particular temporal shape is in close accordance with experimental conditions and observations for the arc phase (see results section). The short breakdown with its δ-function-like shape is not accounted for because of the low energy deposited by this phase. The ignition system was designed to deposit less than approximately 10% of the total spark energy during the breakdown phase although the conversion efficiency of this phase is the highest [11]. This was confirmed experimentally by calorimetric measurements using sparks consisting only of the breakdown (with the constant power supply generating the arc phase switched off, see next section) and using sparks consisting of the breakdown and the arc phase.

Calculations were performed for stoichiometric CH_4–air mixtures using a detailed reaction mechanism consisting of 34 chemical species and 295 elementary reactions [12]. The mixture was assumed to be homogeneous and quiescent initially.

Thermodynamic properties were taken from the JANAF tables [23]. Calculations were performed for similar timescales as the experiments (≤ 10 ms).

2 Experimental

2.1 Spark ignition system

The electric ignition system was designed and built at the Institut für Technische Verbrennung, University of Stuttgart, following the concept published in [7]. The main focus of the design was to ensure highly reproducible spark characteristics. Following an external trigger, a high-voltage source delivered a pulse (whose amplitude depended on the electrode distance) producing a conductive plasma channel between the tips of two tungsten electrodes (breakdown phase). The energy of this phase was kept above a threshold where stable operation was ensured. On the other hand the energy release during the breakdown phase was kept well below the minimum ignition energy. Because the major amount of energy is deposited during the much longer arc phase ($\sim 200\,\mu$s) pressure inhomogeneities are equilibrated efficiently over the whole combustion volume and shock waves can be neglected. Thus the uniform pressure assumption can be used in the numerical simulation [20, 24].

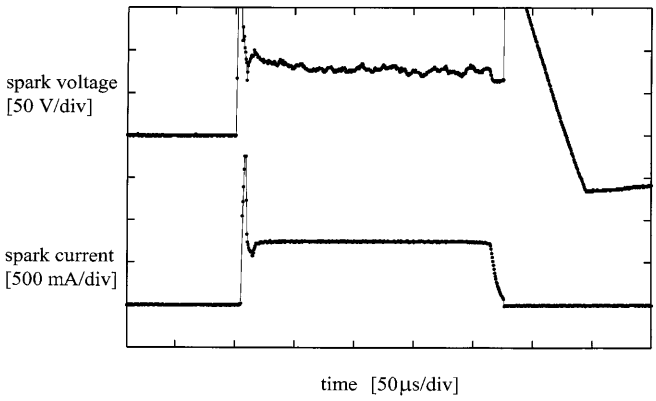

Fig. 1. Temporal profiles of electrode current and voltage measured during a typical electrical discharge. The high peak at the leading edge is due to the short breakdown phase which could not be time-resolved by the probes used here. The voltage rise at the end of the spark (marked by the falling edge of the current trace) is of no relevance for the electrical spark energy and is therefore not especially examined

After the discharge of the electrode capacitance (giving rise to breakdown), the electrical resistance of the plasma channel drops under a certain threshold. The length of this phase is approximately 150 ns as measured by plasma emission using the framing camera which is described in a subsequent section. During the breakdown phase a constant-current power supply is switched on. It supplies user-selectable currents between ~ 0.5 and ~ 1.5 A with resulting electrode voltages of ~ 80 to ~ 120 V. This corresponds to typical values for commercial ignition systems [2]. The arc phase can be sustained for arbitrary times up to a maximum of 500 μs. By use of a series of fast Darlington circuits the electrical current passing the plasma can be kept constant within a few percent. These circuits accomplish an automatic adjustment of the potential drop across the electrode gap according to the prevailing resistance in the plasma. Switching to a glow discharge as described in [25] was never observed in the present experiments. Typical traces for current and voltage measured during an ignition process are shown in Fig. 1. After the breakdown phase the well-defined top-hat profile for the arc phase can clearly be seen. The circuit achieved a current reproducibility of better than 2% (single-event standard deviation from mean). This reproducibility is crucial for a meaningful comparison with results from modelling where data from several independent ignition events has to be considered.

2.2 Combustion vessel

The constant-volume combustion cell consisted of a cylindrical vessel (diameter 15 cm, height 16 cm) with three optical access ports equipped with quartz windows as shown in Fig. 2. It is similar to the system presented in [26]. Two tungsten electrodes (diameter 1 mm) point from opposite ends along a vertical axis towards the centre of the vessel. The electrode tips are sharpened in order to define the contact area of the plasma more clearly. Typically a gap of 1 mm between the electrodes was used. The ignition system was mounted as close as possible to the electrodes. Electromagnetic noise was effectively shielded using a double-walled metal housing.

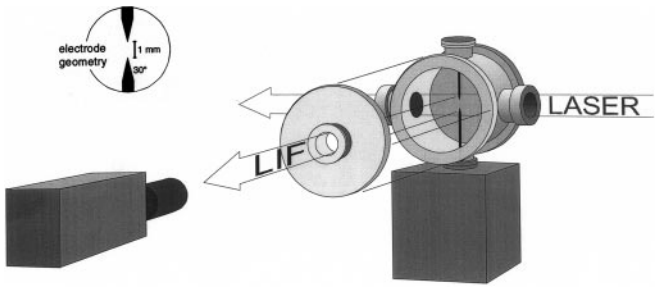

Fig. 2. Sketch of the ignition cell. The electrical ignition system was mounted underneath the vessel as close to the electrodes as possible. The electrodes are made from tungsten wire (diameter 1 mm). The angle of the sharpened electrode tips is approximately 30° (see insert of Fig. 2). The spark occurred near the centre of the vessel. The laser sheet passed in a plane about 1 mm away from the electrodes displayed as the arrow going to the left. Signal detection was at right angles to the laser propagation direction

After a standardised purging procedure and evacuating the chamber to approximately 25 mbar, methane (purity 99.5%) and synthetic air were filled into the vessel. By means of a calibrated baratron (MKS 122) partial pressures of the different reactant gases could be adjusted to an accuracy of about 0.5 mbar. Measurement events occurred on a time period sufficiently large for the vessel temperature to equilibrate between subsequent runs. Wall temperatures were not significantly above room temperature for all experiments reported.

Pressure traces inside the vessel were recorded by a fast piezo-electric pressure transducer (Kistler 6061 B). The discharge voltage was measured using a standard voltage probe (Tektronix P6015). Currents were measured using an earthed pick-up resistor. Voltage and current traces were stored on a digital oscilloscope for subsequent data processing. A low-pass filter at the input of the oscilloscope prevented destructive voltage peaks during the breakdown phase.

2.3 The laser system

The details of the laser system are described in more detail elsewhere [27]. The laser system consisted of 4 individual Nd:YAG oscillator/amplifier units (B.M. Industries, France) each one capable of switching the Pockels cell twice during the duration of the flashlamp pulses (double-pulse operation, DPO). In this way each unit was capable of delivering up to two pulses with a selectable delay of between ~ 25 and 145 μs. Thus a maximum of 8 pulses was obtainable from the system which could be independently triggered to arbitrary external events. The output beams were frequency doubled and combined using a patented beam combination scheme (B.M. Industries, France) resulting in a pulse train propagating as a single beam. Pulse energies at 532 nm were around 600 mJ per pulse if the laser was run at 1 pulse per cavity (total of four pulses) or around 270 mJ per pulse in DPO mode.

A single dye laser system (Continuum) operating on Rhodamine 590 dye containing methanol solutions was pumped with this laser pulse train. Although capable of running at MHz repetition rates, typical timescales of interest in the present study were of the order of 1 ms. Since this corresponded to a time interval longer than the flashlamp pulses of the pump laser system, no additional information was obtained from the second pulse in the DPO mode. Therefore the

pump laser was operated in the single-pulse mode and only four sequential PLIF images were recorded out of a possible total of 8.

The dye laser output was frequency doubled using a single type-I phasematched KDP crystal. The intensity and spatial mode of the resulting doubled radiation was degraded for later pulses within a pulse series. This is attributed to thermal dissipation and refractive index variations in the dye laser and has been discussed in [27]. The shot-to-shot stability and the relative energies in the output pulses were monitored on a fast silicon PIN diode and optimised by adjusting the relative dye laser pulse energies accordingly, generally adjusting for increasing power as the series progressed. This was achieved using variable waveplate/polarizer assemblies in each of the oscillator sections of the pump laser and in this way changing the relative pump powers for the individual dye laser pulses.

Typically around 4 mJ per pulse around 283 nm were obtained with relative pulse to pulse fluctuations of the order of about 20 percent which made online intensity measurements mandatory. The wavelength was tuned to the $Q_1(8)$ transition in the $v'' = 0, v' = 1$ band of the $A\,^2\Sigma^+ \leftarrow X\,^2\Pi$ system of OH checked by performing OH spectral scans in a laboratory-scale Bunsen-type flame. For all experiments the detected OH fluorescence corresponded to emission in the 1,1 and 1,0 bands near 310 nm. The linewidth of the laser was about $0.2\,\mathrm{cm}^{-1}$. This light was spatially filtered and focused into a light sheet using a cylindrical quartz telescope consisting of two positive 200-mm-focal-length cylindrical lenses and a -40-mm negative cylindrical lens. The dimensions of the light sheet were approximately 45 mm in height and 0.2 mm in thickness. To reduce stray light from light scattered off the electrodes the light sheet was displaced by 1 mm from the electrodes towards the camera detector.

For the concentration measurements described, laser sheet profiles were recorded online which could be used to normalise PLIF data on a shot-by-shot basis. For this purpose, a reflection of the laser sheet was directed into a cell containing fluorescing dye. The resulting LIF signals were imaged onto the detector concurrently with the OH PLIF images which were subsequently divided by this profile. Both OH and dye PLIF signals were checked for linearity with laser power prior to measurements.

2.4 The detector

The detection system consisted of a modified Imacon 468 framing camera (Hadland Photonics, UK). The system featured 8 independent intensified CCD detectors (ICCD) with 384 times 576-pixel arrays and 8-bit dynamic resolution. Individual events were imaged onto the individual arrays by use of a Cassegranian prism beam-splitter built into the camera system. To increase the overall gain of the system and to make it UV-sensitive an additional three-stage intensifier module was attached to the optical input of the camera prior to the prism beam-splitter. This intensifier could be operated at repetition rates of up to 1 MHz. The electronics of the camera were modified to allow flexible triggering of the intensifiers to arbitrary external events. The master trigger and all subsequent trigger pulses from which the ignition system, the lasers, and the camera heads were triggered were derived from two 4 channel pulse generators (Stanford).

3 Experimental results

3.1 Method of image analysis

Figure 3 shows a typical sequence of four OH PLIF images obtained during the experiments. The data shown were obtained for a stoichiometric mixture of methane and air at atmospheric pressure. Since the series displayed corresponds to one single-ignition event tracked sequentially in time, one can think of the data as a 'movie' featuring the time development of the OH concentration field. In the example shown, the time separation between images corresponds to 2 ms. The circular wedge marked out on the last image of the series marks the data used to find flame radii and propagation speeds (see below).

The laser sheet position was displaced approximately 1 mm from the spark electrodes which lie in a plane parallel to the picture plane and which point into the vertical direction of the picture. The excellent quality of the PLIF images is apparent, with signal-to-noise ratios exceeding 50 to 1 for the largest signals seen. From such sequences flame velocities can be calculated with high precision using the methods outlined below. Near the flame front OH concentration gradients are seen to be very steep falling off gradually towards the centre of the image. OH concentrations are lower in the vicinity of the electrodes indicating flame quenching in these regions. Furthermore, the flame propagation is slower in a direction along the electrode axis, leading to an imperfect circular shape as combustion proceeds. As discussed above, only data along a line perpendicular to the electrode axis were compared to the results from the simulations. Along this line, effects of the electrodes on mass and heat transport are minimal thus minimising the error associated with the one-dimensional approximations used in the calculations.

The position of the flame front was determined from the experimental images as follows: First, individual images from a series were corrected for relative image displacements and distortions. This was done by recording an alignment matrix containing 5 reference points with co-ordinates (x_i, y_i) with the 8 camera channels j. A reference channel was then deter-

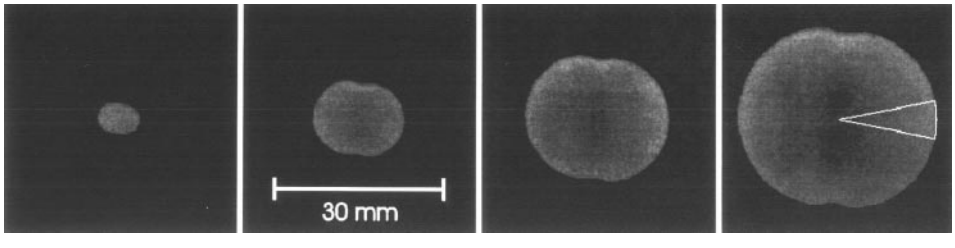

Fig. 3. Series of four single-shot PLIF images of OH corresponding to a single ignition event. The sequence covers times from 1.35 to 7.35 ms, time separations between images are 2 ms. The circular sector superimposed on the last image marks out flame front and radius along a direction perpendicular to the electrode axis as obtained by the image analysis software described in the main text

mined which was obtained by calculating

$$d = \sum_{i=1}^{5} \sum_{j \neq r} \sqrt{(x_{i,r} - x_{i,j})^2 + (y_{i,r} - y_{i,j})^2} \quad (3)$$

for each of the five points of the alignment matrix. Here r refers to the reference channel number, j takes on all other channel values. The channel r for which d was a minimum (in our case channel 3) was used as the reference for the distortion corrections. Because it was necessary to shift images from different channels with respect to each other this procedure ensured the minimum loss of image information. By using a least-squares fitting routine which minimises the expression above, the coefficients of a second-order transformation matrix T_j were determined for each channel j which could then be used to map $x_{i,j} \rightarrow x_{i,r}$ and $y_{i,j} \rightarrow y_{i,r}$. By operating with these transformation matrices on entire images relative distortions and shifts between individual channels could be eliminated. All experimental images were subsequently transformed using the T_j values determined in this way. Notice that this procedure is valid even if the camera is moved or refocused because the effective object plane is given by the position of the first image intensifier which is fixed. The relative displacement between images was below the camera resolution after applying this procedure.

Subsequently the images were divided into sixteen 22.5° angular sectors starting from an initially 'guessed' centre point from which the flame propagated. One such sector is shown in Fig. 3, image 4. Within each sector the intensities of pixels corresponding to the same radial distance to the centre were averaged which resulted in a radial intensity distribution of the sector. From such distributions the position of the flame front was determined from the falling edge of this radial intensity distribution. For this purpose the intensity distribution was differentiated, filtered, and a Gaussian curve fitted to the derivative. The centre of this Gaussian was taken as the flame front position. The choice of the flame centre position was crucial, thus the entire procedure was employed iteratively to establish the flame centre precisely. Finally, only values obtained from sectors perpendicular to the electrode axis (such as shown in Fig. 3) were used for comparisons with modelling results.

3.2 Flame front propagation

The speed of the radial flame front propagation v was calculated by determination of the relative difference in flame radius from sequential PLIF images and dividing this by the time difference corresponding to these events. The relative error in the speed v calculated from the recorded OH images is given by

$$\frac{\sigma_v}{v} = \sqrt{\sum_i \left(\frac{\sigma q_i}{q_i}\right)^2}, \quad (4)$$

where $\sigma q_i / q_i$ is the relative error in the independently measured quantity q_i. The total error is a combination of errors in the estimation of the flame radius by the image analysis method, the error in the calibration of the image scale, and the error in the time measurement between individual frames. The largest error resulted from the determination of the radius. The combined relative error in the speed of the radial flame front propagation was found to be 1.4%.

4 Modelling results

4.1 Initial conditions

From the pressure trace obtained experimentally it can be seen that within the first 8 ms after $t = 0$ (beginning of discharge) the pressure remains unchanged (1013 mbar). Therefore a temporally constant pressure could be assumed in the calculations. Since early in the process the volume of burnt gases is much smaller than the volume of the vessel, the exact geometry of the vessel is of no importance to the flame propagation at this early stage. The mixture ($\lambda = 1$), the length of the arc phase (200 μs), and the initial temperature of the gas mixture (300 K) used in the calculations were determined experimentally. An initial radius (beginning of the arc phase) of 100 μm was assumed for the plasma channel as estimated from spark emission measurements and in accordance with [6]. Quantitative modelling concerning the efficiency of electrical to thermal energy transfer to the gas phase and the amount of heat loss to the electrodes is very difficult [28]. For this reason in the simulation the intensity of the arc was adjusted to result in a maximum plasma temperature during this phase of approximately 4500 K, in close agreement with values reported in [6]. This was achieved by using an energy density of $D_s/\tau_s = 1500\,\mathrm{J\,m^{-1}s^{-1}}$ in (1). In this study no effort has been undertaken to measure the plasma temperatures experimentally.

4.2 Computational results and comparison with experimental data

Because of the use of a detailed model, information about all chemical and physical parameters involved in the process is available. Comparison, for example, with the measured OH profiles is therefore directly possible. Figure 4 depicts OH profiles for different times after the beginning of ignition. During the spark the high peak temperature of approximately 4500 K results in large OH mole fractions (up to 4.5%). Because of the short time scales involved, an extremely high gradient of OH mole fraction at the surface of the plasma results. A growing flame kernel can be observed after approximately 100 μs. When the spark is switched off the OH mole fraction drops near $r = 0$ due to heat conduction from the spark-heated volume to its surrounding. However, residual OH generated in the initial plasma phase has an influence on the radial concentration profile well into the temporal region where the flame kernel has developed. Elevated OH mole fractions at $r = 0$ are evident at times until approximately 3 ms after the spark has diminished. This temporal decay of the plasma generated OH is a manifestation of heat conduction and species diffusion processes. The loss of heat effected by the former shifts the chemical equilibrium position towards a lower OH mole fraction.

Using the data displayed in Figs. 3 and 4 the flame propagation in time can be extracted. The result is shown in Fig. 5:

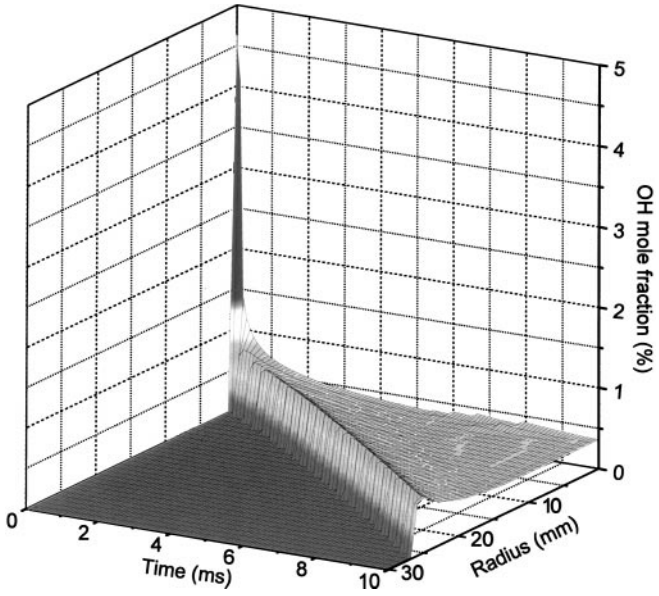

Fig. 4. Simulation of the temporal evolution of the mole fraction of OH radicals. A spark intensity of $D_s/\tau_s = 1500\,\mathrm{J\,m^{-1}s^{-1}}$, a spark diameter of 200 μm, and a duration of 200 μs were used for the calculations. The OH edge marks the approximate location of the flame front in time. Note the enormous OH peak near $t = 0$ where the spark occurs. This initial peak decays rapidly although it affects equilibrium concentrations in the burnt phase for a few ms after the spark has occurred (see main text). The irregular structure between 6 and 8 ms around $r = 0$ mm is due to a limited number of spatial grid points and the adaptive regridding procedure

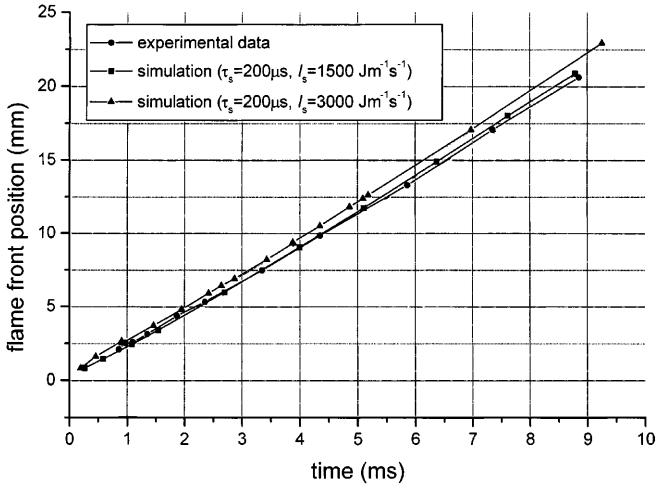

Fig. 5. Comparison between experimental data and computational results. The flame front position is defined as described in the results section. Calculations are shown for two spark intensities at $D_s/\tau_s = 3000\,\mathrm{J\,m^{-1}s^{-1}}$ (*triangles*), and $D_s/\tau_s = 1500\,\mathrm{J\,m^{-1}s^{-1}}$ (*squares*), respectively. The latter, corresponding to a core temperature of the plasma during the arc phase of 4500 K, gives a better agreement with the experimental results

circles on the graph show the development of the flame position as obtained experimentally from the PLIF data, superimposed are the results from the calculations. The simulations correspond to spark intensities of $1500\,\mathrm{J\,m^{-1}s^{-1}}$ (squares) and, for comparison, also $3000\,\mathrm{J\,m^{-1}s^{-1}}$ (triangles). Spark durations were 200 μs in both cases. It can be seen from the graph that the flame speeds (proportional to the slopes of the curves) are not sensitively dependent on the spark energy used. On the other hand a higher spark intensity results in a higher initial temperature. Within the uniform-pressure assumption and assuming a similar size of the plasma channel, this results in a larger gas expansion. Consequently growing of the subsequent flame kernel starts from a larger initial radius and this explains the displacement of the two curves seen.

4.3 Error estimation

The numerical scheme is based on a time integration with an error control which keeps the error below 0.1%. Furthermore, adaptive gridding minimises the error associated with spatial discretisation. Errors in the present approach are mainly due to the restriction to a one-dimensional geometry neglecting heat losses to the electrodes. To account for this, the amount of source energy has to be adjusted to result in a "meaningful" temperature as given in the literature. The approach is limited to cases where the breakdown does not cause a strong shock wave, which would lead to considerable recirculation as a consequence of the shock and rarefaction wave [29]. By limiting the content of the breakdown to approximately 10% of the total spark energy the influence of a shock wave is effectively suppressed in the present case as discussed earlier. Furthermore severe heat losses to the electrodes and recirculation may result in a toroidal instead of the spherical flame shape. For the present case (as seen from Fig. 3) this is of minor importance for the spark characteristics used leading to the results presented here. But a pronounced deviation has indeed been observed when using an extremely short, or, no arc phase: Here the ignition kernel became fully toroidal in shape. This fact shows the limits of the currently employed one-dimensional model of the process. A full, two-dimensional simulation of the current geometry is currently under development [28].

5 Discussion

Flame propagation in closed vessels using geometrically centred spark ignition of quiescent combustible mixtures has already been investigated by several researchers [6, 7, 13–15, 30]. Often burning velocities were extracted from measured pressure traces. With this method, however, no information can be obtained on the early stage of flame growth because a measurable pressure rise is not observed until a significant portion of the load has already burned up.

Data of this study were compared to findings from other researchers. Results reported in [30], obtained in a vessel of comparable dimensions, seem to represent an almost exact continuation of the trends observed in the present case albeit for later times (see Fig. 6). Using time-resolved interferometry Maly et al. [6] investigated diameters and expansion velocities for propagating as well as extinguishing flames. They focused mainly on very early times of the process where the spark is still activated. In this regime, where extreme density and thus refractive index gradients are present, interferometric methods perform very well. Data presented in [6] corresponding to the present mixtures, is reproduced in Fig. 6 for comparison. Although discharge conditions in [6, 30] were different to those reported here, the data measured in the present study fill up the gap between these more recent investigations very well as evident from Fig. 6. Looking at the

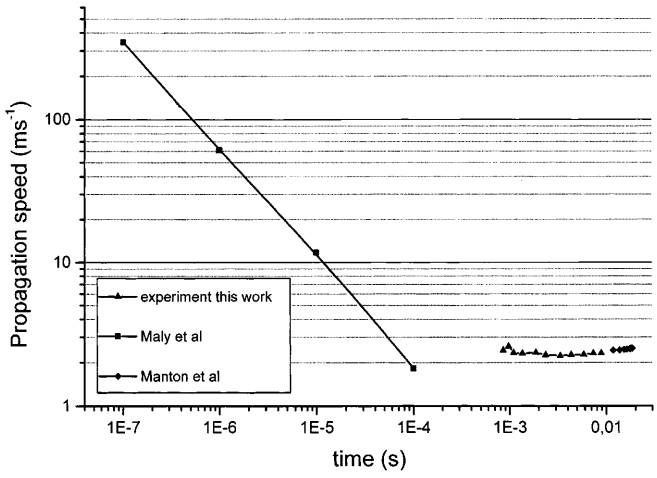

Fig. 6. Speed of spark expansion velocity and subsequent flame propagation, respectively, for initially quiescent methane/air mixtures. *Squares* indicate expansion velocities as obtained by Maly et al. [6]. *Diamonds* correspond to measurements by Manton et al. [30]. Measurements as obtained in the present work are indicated by triangles

temporal evolution of the flame speed (Fig. 6) it is interesting to note a slight increase with time which is clearly exhibited by the model (compare Fig. 4). This is caused mainly by the effect of curvature on the flame front [31].

The excellent quality of the OH PLIF data obtained allowed the extraction of relative OH concentrations which could be compared directly with the modelling data. Figure 7 shows an example of this. Displayed is a cross-sectional profile from a single-shot OH PLIF image (displayed as solid dots), along a line centred in the spark gap and in a direction perpendicular to the electrodes. The trace corresponds to image 4 in Fig. 3. Although the data has not been corrected for collisional quenching, which decreases the fluorescence quantum yield, it represents a good representation of the actual relative OH concentration. In the burnt gases of hydrocarbon flames the quenching rate is nearly constant [32] and no corrections have to be made. Variations are expected only near the flame front, where steeper temperature (and thus

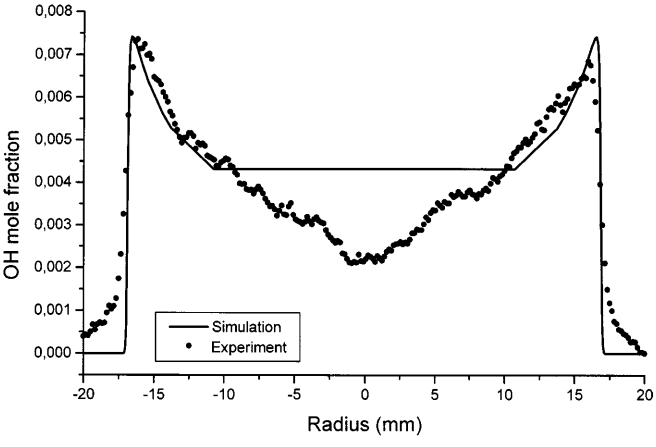

Fig. 7. Comparison of OH concentration profiles obtained from OH PLIF data with results from simulations. The profile corresponds to 7.35 ms after ignition and is taken along a line perpendicular to the electrodes and centred in the spark gap

density) gradients exist, although the effect is small for the present flame (a maximum of 20% [33]).

The experimental profile was scaled in height until it matched the corresponding theoretical profile (solid line), no scaling along the spatial co-ordinate was made. The theoretical data represent the measurement very well, particularly the steep concentration gradients near the flame front and the subsequent fall off towards the burnt gas side. Near the centre, experimental concentrations are significantly lower than theoretical ones (by nearly a factor of two). This is a manifestation of cooling effects near the electrodes as discussed above. These are substantial especially at these late stages of the event (≈ 7 ms after ignition for the present example), where heat losses have accumulated over long times. This observation demonstrates the limitations of the one-dimensional approach used. In the wings of the flame, the OH concentrations do not fall off as abruptly as the model predicts. Reasons for this discrepancy are currently under investigation.

6 Conclusions

The present study reports on the investigation of flame propagation in premixed methane–air mixtures by the use of OH PLIF and gives an extensive experimental characterisation and numerical simulation of a spark-ignited, laminar combustion system. The PLIF technique has been used already in the context of spark and laser ignition as reported in [26, 34, 35]. In contrast to previous approaches, measurements presented here were undertaken in a sequential, time-resolved fashion allowing the capture of up to four subsequent snapshots of a single combustion event. The advantage was twofold. First, it allowed the check of possible irregularities within the combustion event. During a later stage of these experiments, where controlled amounts of turbulence were coupled into the system, this feature was especially important [19]. Second, in the present, laminar case it constituted an enormous timesaving compared to conventional, single-pulse approaches. The complicated filling and purging procedures, employed to ensure maximum reproducibility, required a time delay of about 11 min between two successive ignition events. By increasing the number of recorded events per ignition in the way described, the statistics of the experiment could be significantly improved and effects due to long-term drifts in the measurement equipment were minimised.

The measurements conducted proved that the ignition system was capable of delivering well-defined sparks leading in turn to highly reproducible ignition and subsequent flame propagation. A detailed characterisation of the ignition system was presented giving the opportunity to study the influence of turbulence upon the ignition process during a later stage of this project [19].

Current efforts are directed at improvements of the model to take into account plasma kinetics as well as heat losses to the electrodes. The latter requires a two-dimensional approach which is presently being developed [28]. Furthermore, such a model enables a treatment of the recirculation problem (see for example [29]). Flame shapes other than spherical, for example toroidal flame shapes, which frequently occur in spark-ignited combustion, will thus become possible to model in the future.

Acknowledgements. A.D. and S.L. wish to thank P. Besser for support and fruitful discussions concerning the ignition system. The authors are grateful for the assistance of A. Franke in performing the calorimetric measurements. J.H. acknowledges a graduate scholarship by the Swedish Centre for Combustion Science and Technology. Financing of this project by the European Commission under contract number ERBFMGECT-950020 and by the Forschungszentrum Karlsruhe is gratefully acknowledged.

References

1. R.R. Maly: 25th Symposium (International) on Combustion (The Combustion Institute, Pittsburgh 1994) pp. 111–124
2. J.D. Dale, M.D. Checkel, P.R. Smy: Prog. Energy Combust. Sci. **23**, 379 (1997)
3. S. Pischinger, J.B. Heywood: SAE Paper No. 880518 (1988)
4. M. Beyer: SPIE **2506**, 111 (1995)
5. W. Breitung: FZK Nachrichten **29**, 347 (1997)
6. R.R. Maly, M. Vogel: 17th Symposium (International) on Combustion (The Combustion Institute, Pittsburgh 1978) pp. 821–831
7. G.F.W. Ziegler, E.P. Wagner, R.R. Maly: 20th Symposium (International) on Combustion (The Combustion Institute, Pittsburgh 1984) pp. 1817–1824
8. E. Sher, J. Ben-Ya'ish, T. Kravchik: Combust. Flame **89**, 186 (1992)
9. T. Kravchik, E. Sher, J.B. Heywood: Combust. Sci. Technol. **108**, 1 (1995)
10. R.R. Maly: *Fuel Economy in Road Vehicles Powered by Spark Ignition Engines*, ed. by J.C. Hilliard, G.S. Springer (1984)
11. B. Saggau: Arch. Elektrotechnik **64**, 229 (1981)
12. J. Warnatz, U. Maas, R.W. Dibble: *Combustion* (Springer, Berlin, Heidelberg 1996)
13. P.M. Boston, D. Bradley, F.K.-K. Lung, I.M. Vince, F.J. Weinberg: 20th Symposium (International) on Combustion (The Combustion Institute, Pittsburgh 1984) pp. 141–149
14. O.O. Akindele, D. Bradley: Combust. Flame **47**, 129 (1982)
15. M. Kono, S. Kumagi, T. Sakai: 16th Symposium (International) on Combustion (The Combustion Institute, Pittsburgh 1976) pp. 757–766
16. G.G. de Soete: 20th Symposium (International) on Combustion (The Combustion Institute, Pittsburgh 1984) pp. 161–168
17. M. Kono, K. Hatori, K. Iinuma: 20th Symposium (International) on Combustion (The Combustion Institute, Pittsburgh 1984) pp. 133–140
18. B. Lewis, G. von Elbe: *Combustion, Flames and Explosion of Gases*, 3rd edn. (Academic Press, Orlando 1987)
19. A. Dreizler, S. Lindenmaier, U. Maas, C. Kaminski, J. Hult, M. Aldén: in preparation
20. U. Maas, J. Warnatz: Combustion and Flame **74**, 53 (1988)
21. J.O. Hirschfelder, C.F. Curtiss: In *Flame and Explosion Phenomena* (Williams and Wilkins Cp., Baltimore 1949) pp. 121–127
22. P. Deuflhard, U. Nowak: Tech. Rep. SFB **123**, University of Heidelberg (1985)
23. *Thermochemical tables*, NSRDS-NBS 37, U.S. National Bureau of Standards (1971)
24. U. Maas, J. Warnatz: *Dynamics of Reactive Systems Part I* Vol. 113, ed. by L. Kuhl, J.R. Bowen, J.-L. Leyer, A. Borisov, Progress in Astronautics and Aeronautics, AIAA (Washington DC 1988)
25. W.H. Bloss, H. Albrecht, R.R. Maly, B. Saggau, E. Wagner: Automobil-Industrie **4**/**77**, 45 (1977)
26. J. Xu, J. Warnatz: Ber. Bunsen-Ges. Phys. Chem. **97**, 1741 (1993)
27. C.F. Kaminski, J. Hult, M. Alden: Appl. Phys. B **68**, 757 (1999)
28. M. Thiele, J. Warnatz, U. Maas: SAE Paper 1999-01-1178
29. M. Kono, K. Niu, T. Tsukamoto, Y. Ujiie: 22th Symposium (International) on Combustion (The Combustion Institute, Pittsburgh 1988) pp. 1643–1649
30. J. Manton, G. von Elbe, B. Lewis: 4th Symposium (International) on Combustion (The Combustion Institute, Pittsburgh 1953) pp. 358–362
31. Ya.B. Zeldovich, G.I. Barenblatt, V.B. Librovich, G.M. Makhviladze: *The Mathematical Theory of Combustion and Explosion* (Academy of Sciences of the USSR, Consultants Bureau New York 1985)
32. A. Dreizler, R. Tadday, P. Monkhouse, J. Wolfrum: Appl. Phys. B **57**, 85 (1993)
33. H. Becker, P. Monkhouse, J. Wolfrum, R.S. Cant, K.N.C. Bray, R. Maly, W. Pfister, G. Stahl, J. Warnatz: 23rd Symposium (International) on Combustion (The Combustion Institute, Pittsburgh 1990) pp. 817–823
34. T. Heitzmann, J. Wolfrum, U. Maas, J. Warnatz: Z. Phys. Chem. **188**, 177 (1995)
35. A. Dreizler, V. Sick, J. Wolfrum: Ber. Bunsen-Ges. Phys. Chem. **101**, 771 (1997)